Acta Oceanol. Sin., 2017, Vol. 36, No. 5, P. 9–25
DOI: 10.1007/s13131-017-1058-3
http://www.hyxb.org.cn
E-mail: hyxbe@263.net

Meso-scale eddy in the South China Sea simulated by an eddy-resolving ocean model

FENG Baoxin[1], LIU Hailong[2]*, LIN Pengfei[2], WANG Qi[1]

[1] College of Physical and Environmental Oceanography, Ocean University of China, Qingdao 266100, China

[2] State Key Laboratory of Numerical Modeling for Atmospheric Sciences and Geophysical Fluid Dynamics, Institute of Atmospheric Physics, Chinese Academy of Sciences, Beijing 100029, China

Received 2 March 2016; accepted 25 April 2016

Abstract

Mesoscale eddies (MEs) in the South China Sea (SCS) simulated by a quasi-global eddy-resolving ocean general circulation model are evaluated against satellite data during 1993–2007. The modeled ocean data show more activity than shown by the satellite data and reproduces more eddies in the SCS. A total of 345 (428) cyclonic eddies (CEs) and 330 (371) anti-cyclonic eddies (AEs) generated for satellite (model) data are identified during the study period, showing increase of ~24% and ~12% for the model data, respectively. Compared with eddies in satellite, the simulated eddies tend to have smaller radii, larger amplitudes, a slightly longer lifetime, faster movement and rotation speed, a slightly larger nonlinear properties (U/c) in the model. However, the spatial distribution of generated eddies appears to be inhomogeneous, with more CEs in the northern part of SCS and fewer AEs in the southern part. This is attributed to the exaggerated Kuroshio intrusion in the model because the small islands in the Luzon Strait are still not well resolved although the horizontal resolution reaches (1/10)°. The seasonal variability in the number and the amplitude of eddies generated is also investigated.

Key words: mesoscale eddy, eddy-resolving ocean general circulation model, South China Sea

Citation: Feng Baoxin, Liu Hailong, Lin Pengfei, Wang Qi. 2017. Meso-scale eddy in the South China Sea simulated by an eddy-resolving ocean model. Acta Oceanologica Sinica, 36(5): 9–25, doi: 10.1007/s13131-017-1058-3

1 Introduction

The South China Sea (SCS), which is the largest marginal sea in the northwest Pacific, is surrounded clockwise by the East China Sea, the Pacific Ocean, the Sulu Sea, the Java Sea and the Indian Ocean and can exchange water masses with the adjoining bodies through the Taiwan, Luzon, Balabac, Mindoro, Karimata and Malacca Straits. The patterns and variations of the seasonal upper-layer circulation are driven by monsoons with significant influence from the Kuroshio intrusion (e.g., Liu et al., 2008). A basin-wide cyclonic gyre is present in winter, whereas two gyres occur in summer including a cyclonic gyre in the northern SCS and an anti-cyclonic gyre in the southern SCS.

Mesoscale eddies (MEs) are dominant in the SCS as well as in other regions (e.g., Wang et al., 2003; Lin et al., 2007; Liu et al., 2008) and they play an important role in the transport of mass, heat and dissolved chemical substances (e.g., Chen et al. 2012). In the early studies, several seasonal standing eddies have been found, the Luzon Cold Eddy, located northwest of the Philippines from late autumn to early spring (Yang and Liu, 1998; Shaw et al., 1999; Qu, 2000) and eddies located off eastern Vietnam during the southwest monsoon (Wu et al., 1999; Wang et al., 2003, 2004; Chen et al., 2010). An exceptional anticyclonic eddy near the Xisha Islands is also studied by Chu et al. (2014). They found that the eddy can raise the center temperature and the vertical depth and the growth of the exceptional eddy can be attributed to the unusual summer monsoon and current.

Recent researches of the spatial distribution and statistical characteristics of MEs in the SCS were mainly based on the satellite altimetric data. Wang et al. (2000) first studied mesoscale variability in the SCS by using along-track altimetry data. Two narrow bands of significant mesoscale variability were found to exist north of 10°N. The stronger band occurs along the western boundary and the weaker one appears in the central SCS. Wang et al. (2003) summarized the general eddy characteristics of the SCS based on the eight years of merged altimetry data recorded during 1993–2000. They used a geometric eddy identification and tracking method to identify 58 anti-cyclonic eddies (AEs) and 28 cyclonic eddies (CEs), corresponding to 10.8 eddies per year. Employing a similar method, Lin et al. (2007) presented temporal and spatial variation characteristics of MEs in the SCS by using 10-years altimetry data recorded during 1993–2002. Both of these papers focused on strong MEs. Chen et al. (2011) used winding-angle (WA) method (Chaigneau et al., 2008) to identify eddies during the period 1993–2007 and focused on the eddies with amplitude larger than 3 cm. They concluded that these eddies are mainly generated in a northeast-southwest direction and less frequent in the northwestern and southeastern regions of the SCS. The mean eddy radius in their research is 132 km and eddies with radii of 100–200 km account for 64% of all detected eddies. Chen et al. (2015) have investigated properties of deep eddies which have no footprints at the sea surface in the northwestern SCS. They found that the deep eddies significantly increase the velo-

Foundation item: The National Key Program for Developing Basic Science of China under contract No. 2013CB956204; the National Natural Science Foundation of China under contract Nos 41275084 and 41575084; the Strategic Priority Research of the Chinese Academy of Science under contract No. XDA 11010304.
*Corresponding author, E-mail: lhl@lasg.iap.ac.cn

city intensity and enhance the mixing in the deep ocean.

The MEs and their impacts on the atmosphere, current and transport have also attracted much attention. Chow and Liu (2012) have used satellite observations to study effects of eddies on the sea surface temperature and sea surface wind in the northern SCS. Based on the moored current-meter records, seasonal variability of near-inertial kinetic energy related to storms and eddies in the northwestern SCS have been investigated by Chen et al. (2013). Their results show that the divergence and convergence of MEs can affect the complex propagation and distribution of the near-inertial kinetic energy although it originated from the winds. Interactions between eddy and mean flow are also studied by Wang et al. (2015). Propagation of eddies and their role in the transport of heat and salt are also investigated (Zhuang et al., 2010; Chen et al., 2012) by combining the observations and an eddy-resolving model.

As the observational data are limited in both temporal and spatial resolution, eddy-resolving ocean models have become a useful tool for studying MEs. So far, many numerical studies have focused on the generation mechanism of some individual eddies in the SCS, such as Luzon eddy shedding from the Kuroshio through the Luzon Strait (e.g., Jia et al., 2005; Wu and Chiang, 2007) and three long-lived eddies in the northern SCS (Nan el al., 2011). Few studies focused on the spatial distribution and statistical characteristics of MEs simulated by numerical models in SCS. Xiu et al. (2010) studied the characteristics of eddies in the SCS using the results of the Regional Ocean Model System (ROMS) over the Pacific Ocean. In their studies, the number of simulated MEs was nearly the same as those detected by satellite data. Meanwhile, strong eddies generally lasted longer and penetrated deeper than weak eddies by investigating eddy radius, lifetime, magnitude, vertical extent and their possible linear relationships. They mentioned the model had a relatively higher occurrence value (11%) than that (only 5%) in satellite from west of the Luzon Strait to the southeast of Hainan Island roughly along the 1 000 m bathymetry. Lin et al. (2015) also used ROMS to study MEs, but they focused on the three-dimension structures of MEs in the SCS. They also mentioned that the model had higher EKE in the entrance of the Luzon Strait than that in satellite. These two studies suggested the ROMS had some biases around the Luzon Strait to represent the MEs. But the relationship between MEs and inflow from Luzon Strait are left for study.

We recently developed a semi-global eddy-resolving ocean model (Yu et al., 2012; Liu et al., 2014). Before studying the mechanism of MEs, the performance of the model in simulating MEs should be evaluated firstly. The features of MEs in the SCS have been extensively investigated as previously mentioned. Moreover, Hallberg (2013) reported that the (1/4)° horizontal resolution of the satellite data is capable of resolving eddies for the entire SCS basin except for the continental shelf region. This suggests that the merged altimetry data are able to resolve the most important features of the MEs. The SCS therefore was chosen for evaluating the model results.

The objective of this work is to evaluate MEs simulation in the ocean model against the satellite data. We investigate the spatial distribution of the ME generation and termination; the probability density function (PDF) of six major features, i.e., the radius, amplitude, lifetime, moving velocity, rotational velocity and nonlinear parameter, the relationships among these features; and the seasonal variation of the number of MEs generated and their amplitude. The simulated biases around the Luzon Strait and the mean circulation are also discussed. The organization of this paper is as follows. The numerical model and satellite data are described in Section 2. Section 3 introduces the eddy detection and tracking method. The results of the numerical model and satellite eddies are shown in Section 4. Finally, Section 5 summarizes the findings of this study.

2 Model and Data

2.1 *Model descriptions and data*

The quasi-global eddy-resolving ocean general circulation model used in this study is the State Key Laboratory of Numerical Modeling for Atmospheric Sciences and Geophysical Fluid Dynamics/Institute of Atmospheric Physics (LASG/IAP) Climate System Ocean Model version 2.0 (LICOM2.0) (Liu et al., 2012). The eddy-resolving version of the model includes several updates and improvements. The horizontal grids are increased to 0.1° and the vertical layers are increased to 55 layers. The thickness of the first layer is 5 m. In the upper 300 m, 36 uneven layers are present and the mean thickness is less than 10 m. To avoid the singularity of the North Pole in the longitude-latitude grid, the model domain covers only 66°N–79°S, excluding the Arctic Ocean. In addition, biharmonic viscosity and diffusivity schemes are used in the momentums and tracers equations, respectively. The parameterization of eddies from Gent and McWilliams (1990) is turned off in the equations of tracers. Moreover, the parallel domain partition is changed from a one-dimensional method with only meridional-splitting to a two-dimensional method including both zonal and meridional splitting.

The eddy-resolving model was initialized with the observed temperature and salinity (WOA09) and was integrated for 12 years from zero velocity forced by the climatological monthly wind stress and heat fluxes from the Ocean Model Intercomparison Project (OMIP; Roeske, 2001). After the 12-year spin-up experiment, the model was integrated for 60 years, beginning at the end of the 12th year of spin-up integration and forcing by the daily Coordinated Ocean-Ice Reference Experiments (CORE) algorithm and data from 1948 to 2007 (Large and Yeager, 2004). Owing to the lack of a sea ice module in LICOM2.0, the sea ice concentration was determined by using data from the Hadley dataset. The baseline performances of this experiment will be evaluated in a separate paper.

The satellite data used in this study is a gridded merged product of Maps of Sea Level Anomaly (MSLA) from 1993 to 2007, which was produced and distributed by AVISO (http://www.aviso.oceanobs.com/) on the basis of TOPEX/Poseidon, Jason 1, ERS-1, and ERS-2 data (Ducet et al., 2000). The spatial resolution of the satellite data was 0.25°×0.25° and the temporal interval was seven days. The simulated Sea Surface Height Anomaly (SSHA) was computed by deducting the 15 years mean Sea Surface Height (SSH) from the daily SSH output. Then, to make the model and satellite data consistent, the SSHA data were interpolated onto the same 0.25°×0.25° grid, and the data were selected in seven-day intervals.

2.2 *Model circulation evaluation*

Because the upper-layer circulations in the SCS for the present experiment have not been systematically evaluated thus far, we conducted a basic comparison against the satellite data. Figure 1 shows the surface geostrophic circulations in the boreal winter (December–January–February, i.e., DJF) and summer (June–July–August, i.e., JJA) in the SCS for both the satellite and model data. The model can simulate the primary features of surface circulations and their seasonal variability, such as, the strong and seasonal reversed western boundary current offshore Viet-

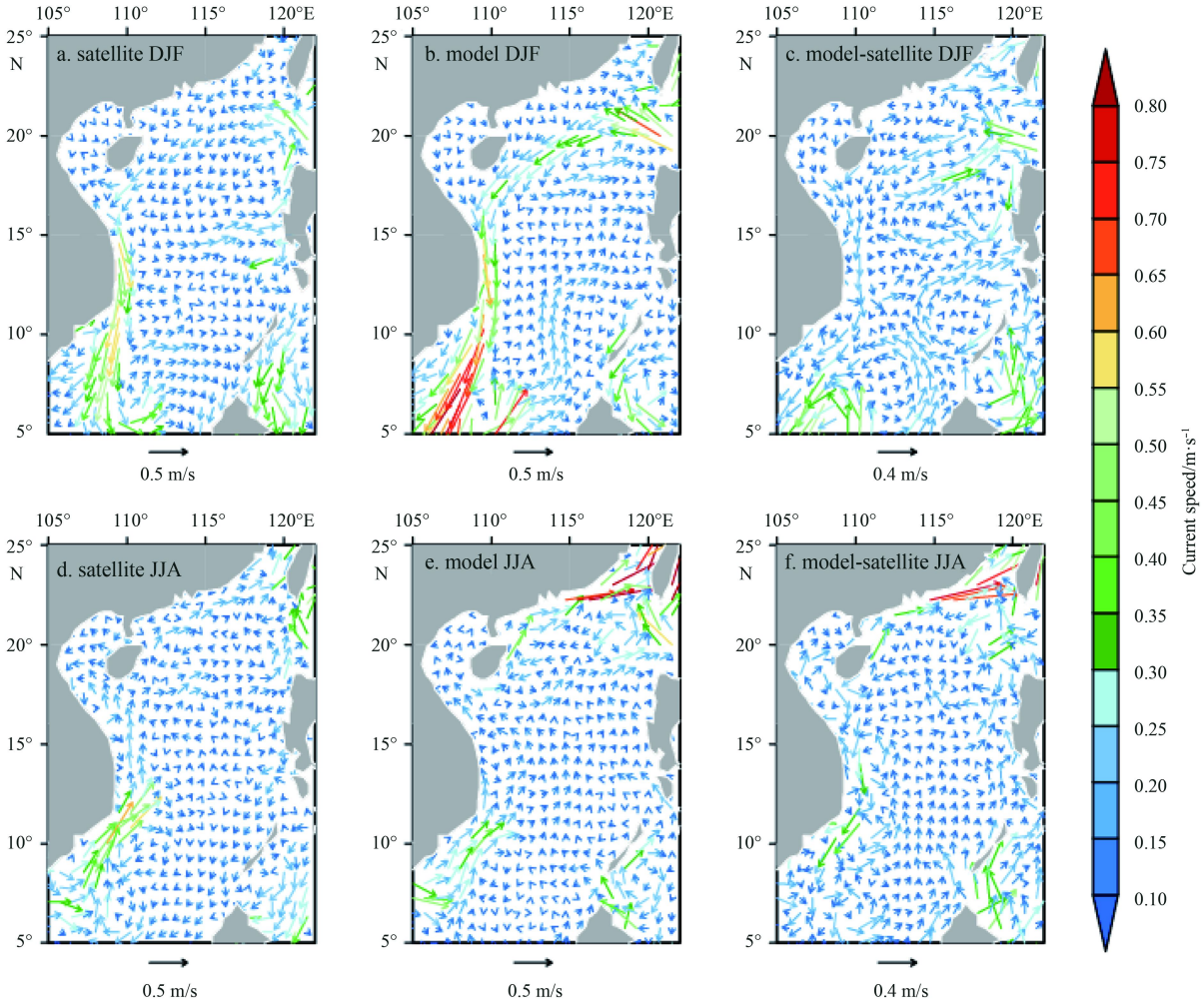

Fig. 1. The winter (a, b) and summer (d, e) upper layer geostrophic circulation (vector) of satellite and model, and the corresponding differences between satellite and model (c, f), respectively. The shaded refers to the speed magnitude of the current.

nam, which flows southward in winter and northward in summer. However, the difference between satellite and model show that the spatial pattern of the surface circulation in the model is significantly more complicated than that in the observations, particularly in the summer season (Figs 1c and f),

The most evident bias of the model is extremely strong Kuroshio intrusion, particularly in winter when the Kuroshio intrusion is strongest in the observation. We attribute this bias to the absence of islands in the Luzon Strait in the model topography, as mentioned by Metzger et al. (2001). In winter, the simulated strong Kuroshio intrusion can reach to the east coast of Vietnam roughly along the 2 000 m isobaths. Thus, it can intensify the southward current along the east coast of Vietnam. The stronger southward current also leads to stronger northward and eastward re-circulation at 110°E to 115°E and at 18°N, respectively. However, the current west of Luzon Island in the model is weaker than that in the satellite. In summer, the Kuroshio intrusion in the model is also stronger than that in the satellite. The majority of the Kuroshio water does not enter the basin scale circulation, but instead flows northeastward through the Taiwan Strait. However, the northward current along the east coast of Vietnam in the model is slightly weaker than that in the satellite.

We also investigated the ability of the model to simulate MEs in terms of eddy kinetic energy (EKE). Figure 2 presents the winter and summer mean EKE in the SCS for the satellite and model. The two boxes indicate the two areas of high eddy concentration in the present study: the North Area (NA, 16.5°–22.5°N, 114°–121°E) and the South Area (SA, 6.5°–15°N, 109°–115°E). Our definition of north and south are generally following Wang et al. (2003), in which they divided the South China Sea into four zones according to the eddy where they have been generated. The north area we defined is the Z1 plus Z2 zones of Wang et al. (2003). The south area is basically the Z4 zone of Wang et al. (2003), but a little bit smaller. These two areas are the regions of high eddy kinetic energy, that is, more eddies are generated and/or occurred in these two areas. The EKE can be calculated from half of the sum of the squared eddy velocity components:

$$EKE = \frac{1}{2}(u'^2 + v'^2),$$

where u' and v' are the geostrophic velocity anomalies deduced from the SLA maps using geographic approximation, $u' = -\frac{g}{f}\frac{\partial(SLA)}{\partial y}$ and $v' = \frac{g}{f}\frac{\partial(SLA)}{\partial x}$, where g is the gravitational constant (g≈9.8 m/s^2) and f is the Coriolis parameter. Two energetic regions occur in the SCS, in the west of Luzon Strait and in the southeast of Vietnam, which is consistent with the results of Cheng and Qi (2010) that high EKE values occurred in the southeast of Vietnam and in the west of Luzon Strait. In general, the model simulated larger EKE than that of the satellite data. In

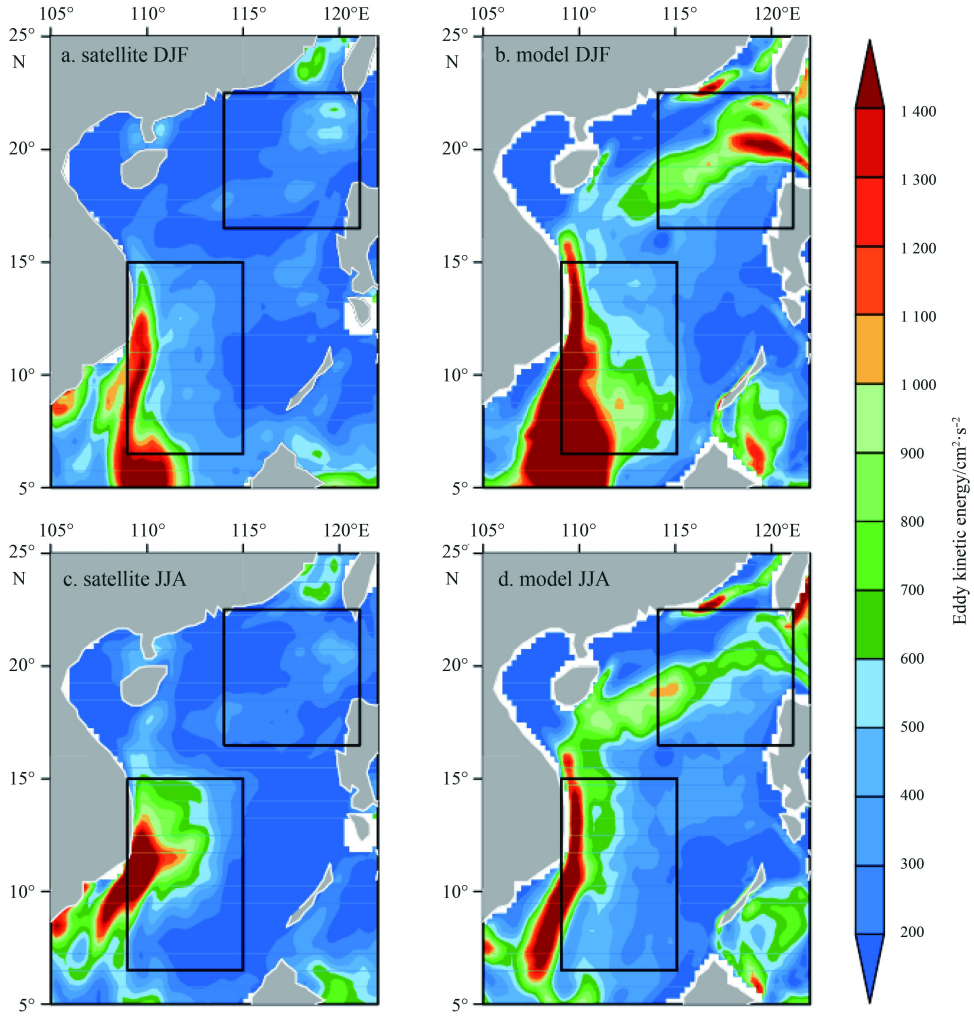

Fig. 2. The winter (a, b) and summer (c, d) EKE of satellite and model, respectively. The black rectangular boxes are the area we focused on: the north area: 16.5°–22.5°N, 114°–121°E and the south area: 6.5°–15°N, 109°–115°E. The unit is cm^2/s^2.

winter, along with the extremely strong Kuroshio intrusion, the EKE belt is larger roughly along the 2 000 m isobaths in the northern SCS close to 18°N. Similarly, in summer, the model shows high EKE in the Taiwan Strait and along the east coast of Vietnam. Zhuang et al. (2010) also shows high EKE values in the west of the Luzon Strait and in the southeast of Vietnam using their ocean models. The comparison of the biases between the mean flow and the EKE suggests that the biases of the mean flow might affect the number and spatial pattern of MEs, which will be discussed in Section 4.

3 Eddy detection and tracking method

Although the Okubo-Weiss algorithm (OW; Okubo, 1970; Weiss, 1991) is widely used in eddy detection, it tends to overestimate the number of eddies (Nencioli et al., 2010; Chaigneau et al., 2008; Souza et al., 2011). After comparing the results obtained from the OW method using the same dataset, Chaigneau et al. (2008) determined that the winding-angle (WA) method can reduce the number of false eddies. Souza et al. (2011) also suggested that the WA method presents the better performance among the three automatic eddy identification algorithms (OW method, WA method and wavelet analysis).

The eddy detection method used in this paper is similar to the WA method (Chaigneau et al., 2009), which has been widely applied in the SCS (Chen et al., 2012), Atlantic Ocean (Chaigneau et al., 2009) and global ocean (Chelton et al., 2011). First, we identified possible CE (or AE) centers by searching for local SLA minima (or maxima) in a moving window of 1°×1° grid points. Then for each possible CE (or AE) center, the algorithm searches for closed contours with an increment (or decrement) of 1 mm. The outermost closed SLA contour, embedding only the considered center corresponds to the eddy edge. Following previous studies (e.g., Chaigneau et al., 2009; Chen et al., 2011), we focused on eddies with amplitudes greater than 3 cm, lifetimes greater than five weeks and water depth greater than 200 m. The eddy tracking method used in this paper is based on the geometrical distance from one eddy center to another (e.g., Isern-Fontanet et al., 2003, 2006). The code written in Matlab is from Lin et al. (2007) with some minor modifications.

When we find the eddy centers and edges, some basic eddy properties can be estimated. Then we define the eddy amplitude as the absolute SLA difference between the eddy center and the eddy edge.

$$Amplitude = |SSHA_{\text{center}} - SSHA_{\text{edge}}| .$$

We further defined the eddy rotation speed U as the mean of the average geostrophic speeds inside the closed contours of the SLA. The moving speed of the eddy c can be calculated by de-

termining the moving distance and the time interval from the results of the eddy tracking. Following Chelton et al. (2011), we defined the nonlinear parameter as *U* divided by *c*.

On average, (45±5.5) eddies per year were identified in the satellite data by using our method (Table 1). These results are significantly greater than those of Xiu et al. (2010) in which only approximately (32.8±3.4) eddies per year were reproduced by the model and (32.9±2.4) eddies per year were observed by satellite. This discrepancy may be attributed to the different eddy detection criteria used in the two studies. Although the OW algorithm tends to overestimate the number of eddies than WA method, Xiu et al. (2010) have imposed additional strict criterions in the OW method to better identify eddies. The modified OW method is much stricter than ours in the present study.

4 Results

4.1 *Eddy genesis and termination*

Figure 3 shows the regional climatology of the eddy generation and termination locations during 1993–2007 for both the satellite and model results. The generated eddies were found nearly throughout the entire SCS basin for both the satellite and model, which is consistent with previous studies (e.g., Wang et al. 2003). Most eddies generated in a northeast-southwest line and southwest of Luzon both for satellite and model, which is consistent with the results of Chen et al. (2011). In general, the model appears to generate a significantly higher number of eddies in the northeastern part of the SCS. The two bands of active MEs by Wang et al. (2000) were also found in the model results but with larger magnitudes. Meanwhile, the eddy generation number changes with latitude; increasing with latitudes and then decreasing sharply north of 13°N for satellite and model (Figs 3c and f). The decreasing is mainly due to exclude the continental shelf where water shallower than 200 m.

A total of 345 CEs and 330 AEs generated for the satellite data and 428 CEs and 371 AEs generated for the model data were identified during 1993–2007 (Table 1). The total number of eddies simulated by the model is approximately 18% more than that observed by satellite. Considering the entire basin, the number of CEs for the model was approximately 24% larger than that for satellite, although the value was only 12% for AEs. Furthermore, we investigated the two regions of eddy concentration. In the NA, the eddy number characteristics for satellite and the model were similar to that in the entire SCS basin: the number of simulated CEs (AEs) was 34% (22%) larger than that for the satellite. However, the value in the SA differed from that in both the entire SCS basin and the NA. The numbers of both CEs and AEs for model in the SA were lower than those for satellite data at approximately 5% for CEs and 36% for AEs. The greater difference between the NA and SA may be related to the intensified Kuroshio intrusion through the Luzon Strait. The detail discussion can be found in Section 5.

The spatial distribution features of eddy termination were similar to those of generation (Figs 3d and e). The eddy termina-

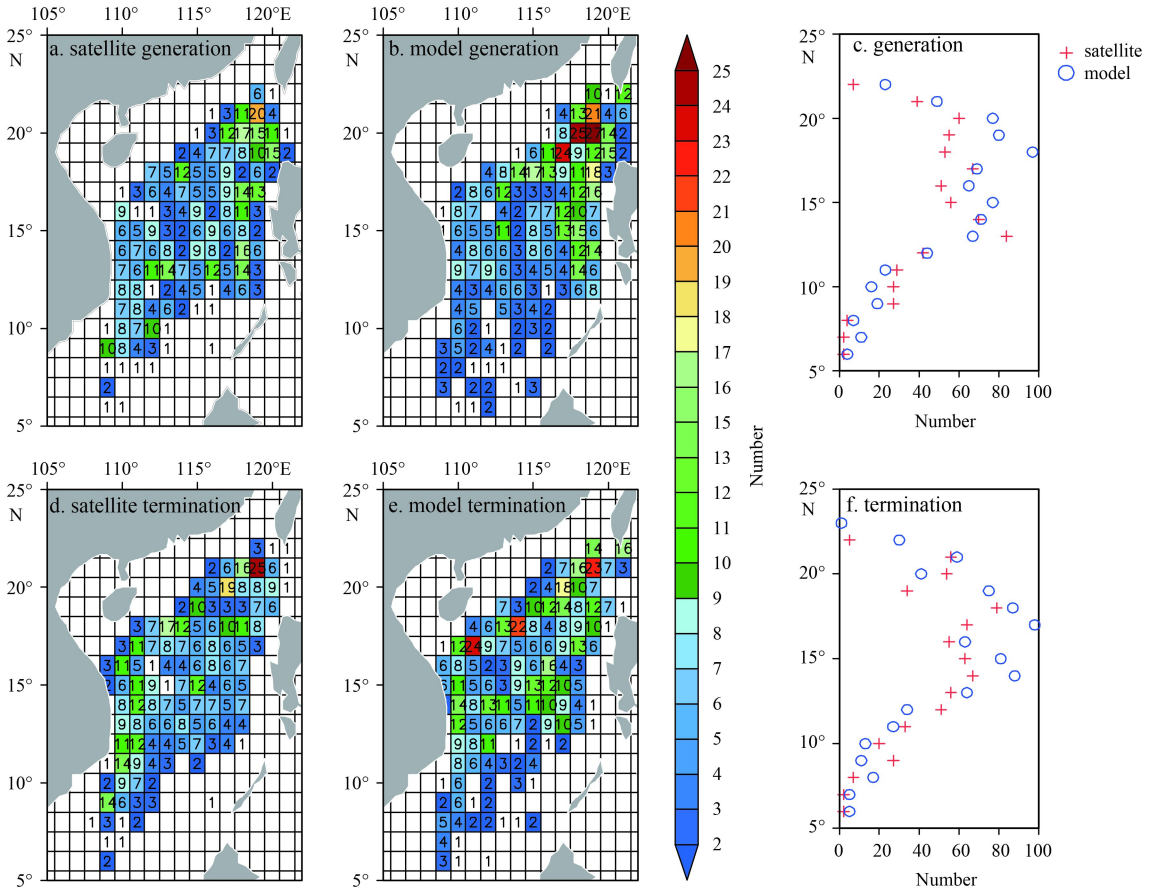

Fig. 3. Regional climatology of eddy generation (a, b) and termination (d, e) locations both for the satellite and the model data in the period of 1993 to 2007. Units are the number of events. Meridional variation of the total eddy generation and termination number for satellite and model (c, f).

Table 1. The generation number of CEs and AEs for satellite, LICOM model and two sensitive experiments in the entire basin, north and south area, respectively

	Experiments	Total	AE	CE
SCS	Satellite	675	330	345
	LICOM	799 (18%)	371 (12%)	428 (24%)
North	Satellite	292	143	149
	LICOM	375 (28%)	175 (22%)	200 (34%)
South	Satellite	185	94	91
	LICOM	146 (–21%)	60 (–36%)	86 (–5%)
Sensitive experiments				
SCS	Exp1	126	50	76
	Exp2	144 (14%)	57 (14%)	87 (14%)
North	Exp1	75	25	50
	Exp2	70 (–7%)	33 (32%)	37 (–26%)
South	Exp1	21	7	14
	Exp2	35 (67%)	10 (43%)	25 (78%)

tion also showed an increasing with latitude first from north to south and decreasing then. However, in the southwest of Luzon, little eddies terminated there. The other characteristics in the eddy termination were all similar to those in their generation.

To present the spatial pattern of eddies more clearly and quantitatively, the eddy generation probability (EGP) of the satellite and the model for CEs and AEs, which is defined by the number of MEs generated per year in a 1° grid, are shown in Fig. 4. Overall, the model was able to simulate the general spatial pattern of eddy generation. For CEs (Figs 4a and b), compared with the satellite, the model generated more eddies in the NA, just west of the Luzon Strait. The maximum value was approximately 1.2 per year for the model, but 0.8 per year for the satellite data. The mechanism of eddies generated in this region has been discussed in previous studies: wind stress curl variation (Yang et al., 2013), the frontal instability of the Kuroshio intrusion (Wang et al., 2000), vorticity advected westward from the Kuroshio front (Liu and Su, 1992), shed from the Kuroshio (Li et al., 1998; Wang et al., 2008b), and the winter orographic wind jets (Wang et al., 2008a). For the model results, the extremely strong westward current west of the Luzon Strait related to the Kuroshio intrusion may have led to large velocity shear, both vertical and horizontal and therefore generation of the large number of CEs (Fig. 1).

In addition to the generally large EGP in the eastern basin of the SCS, two discrepancies in the AEs spatial pattern were evident in the model (Figs 4c and d). First, the model results showed a band stretching from west of the Luzon Strait to southeast of Hainan Island roughly along the 2 000 m isobaths. This band is not clearly visible in the satellite map. Second, the satellite data

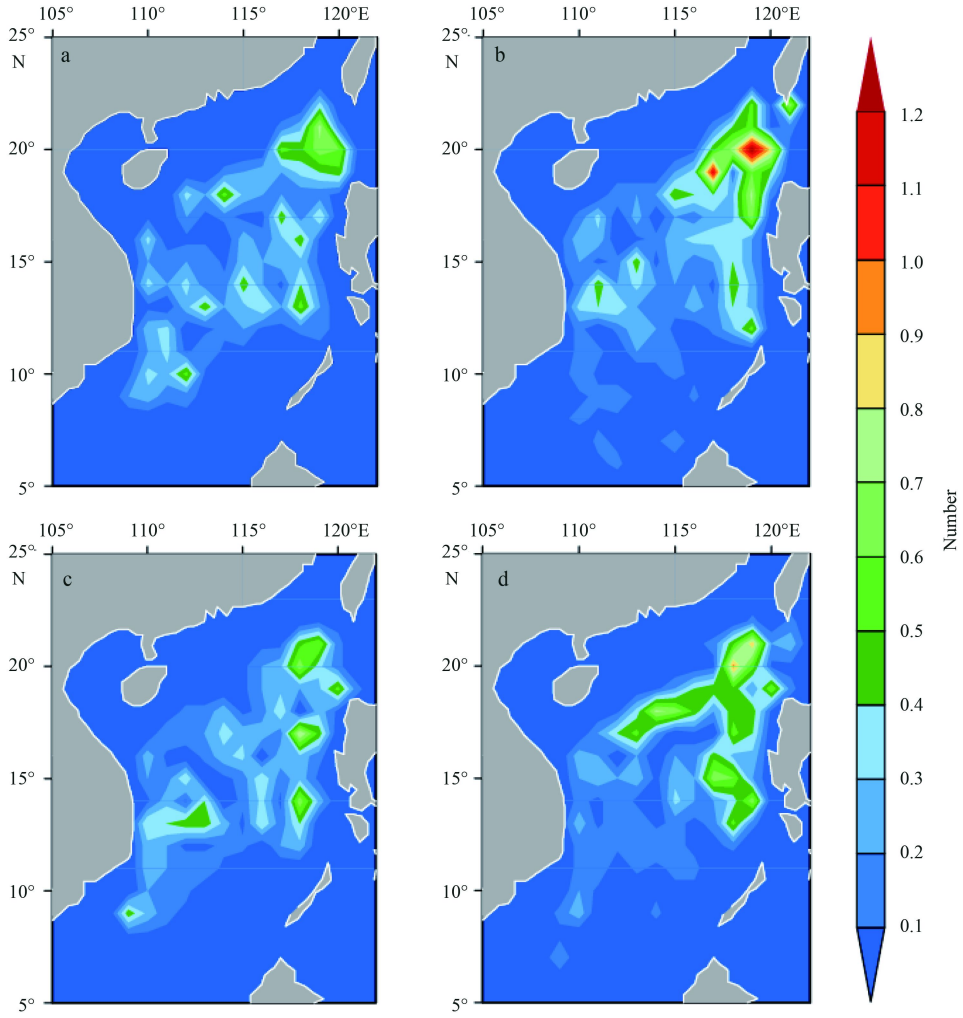

Fig. 4. The generated probability (number per year) of CEs of the satellite (a) and model (b) and probability of AEs of satellite (c) and model (d), respectively.

showed a high EGP value of approximately 0.4 per year offshore Vietnam, whereas a small value of approximately 0.2 per year appeared in the model results. The eddy generation mechanism offshore Vietnam is the dipole wind stress curl in summer (Chen et al., 2010) and strong flow variability (Gan and Qu, 2008).

In general, the model tended to generate more eddies in the SCS. However, the spatial distribution was inhomogeneous, with more CEs in the NA and fewer AEs in the SA. The higher number of eddies in model may be related with the configuration of the model. The horizontal resolution of the model, the temporal frequency and spatial resolution of the forcing and some parameterizations (such as the horizontal viscosity and diffusivity schemes) may all affect the simulation of eddies. The significantly higher resolution and lower horizontal viscosity of the model are likely the main factors; however, the inhomogeneity may be related to the exaggerated Kuroshio intrusion in the model.

4.2 *Eddy characteristics*

To evaluate the model performance, we compared the primary properties of eddy activities between the model and satellite data for the entire SCS basin and the NA and SA where eddies are frequently generated. The PDF of the basic eddy properties including radius, amplitude, lifetime, moving speed (velocity and c), rotation speed (U), and the nonlinear parameter U/c for the entire SCS basin and the NA and SA are shown in Figs 5, 6 and 7, respectively. The top (lower) panel shows the results for the CEs (AEs). The mean values of all the characteristics are shown in the figures.

For the entire basin, the MEs simulated by the model, whether AEs or CEs, tended to have smaller radii, larger amplitudes, slightly lifetimes, faster moving and rotation speeds and slightly larger nonlinear properties (U/c) than those of satellite data. The differences of these properties between the satellite and the model were significant in the 95% confidence interval except lifetime and nonlinearity of AEs. However, the basic properties of eddies in the NA and SA differed in some aspects.

In general, the PDFs of the eddy radii for both the satellite and model had a roughly Rayleigh distribution with slight asymmetry (Figs 5a, 5g, 6a, 6g, 7a, and 7g). The mean radius of CEs (AEs) was 173.5 km (191.1 km) for the satellite data and 153.2 km (169.1 km) for the model in the entire SCS basin. Because the radii of the eddies decreased with an increase in latitude, the radii were smaller in the NA than those in the SA; the same was true for the simulation. The smaller radius of the model may also indicate that the viscosity coefficient is small in the model. The PDFs of the model were more likely to shift leftward; that is, more small eddies were generated in the model. We further investigated the spatial distribution of the small eddies with radii less than 100 km (Figs 8a and b). Nearly all of the small eddies appeared in the NA, and the number of those for the model 61, was significantly larger than that for the observation 14. This result also suggests that the strong Kuroshio intrusion may be related to the errors.

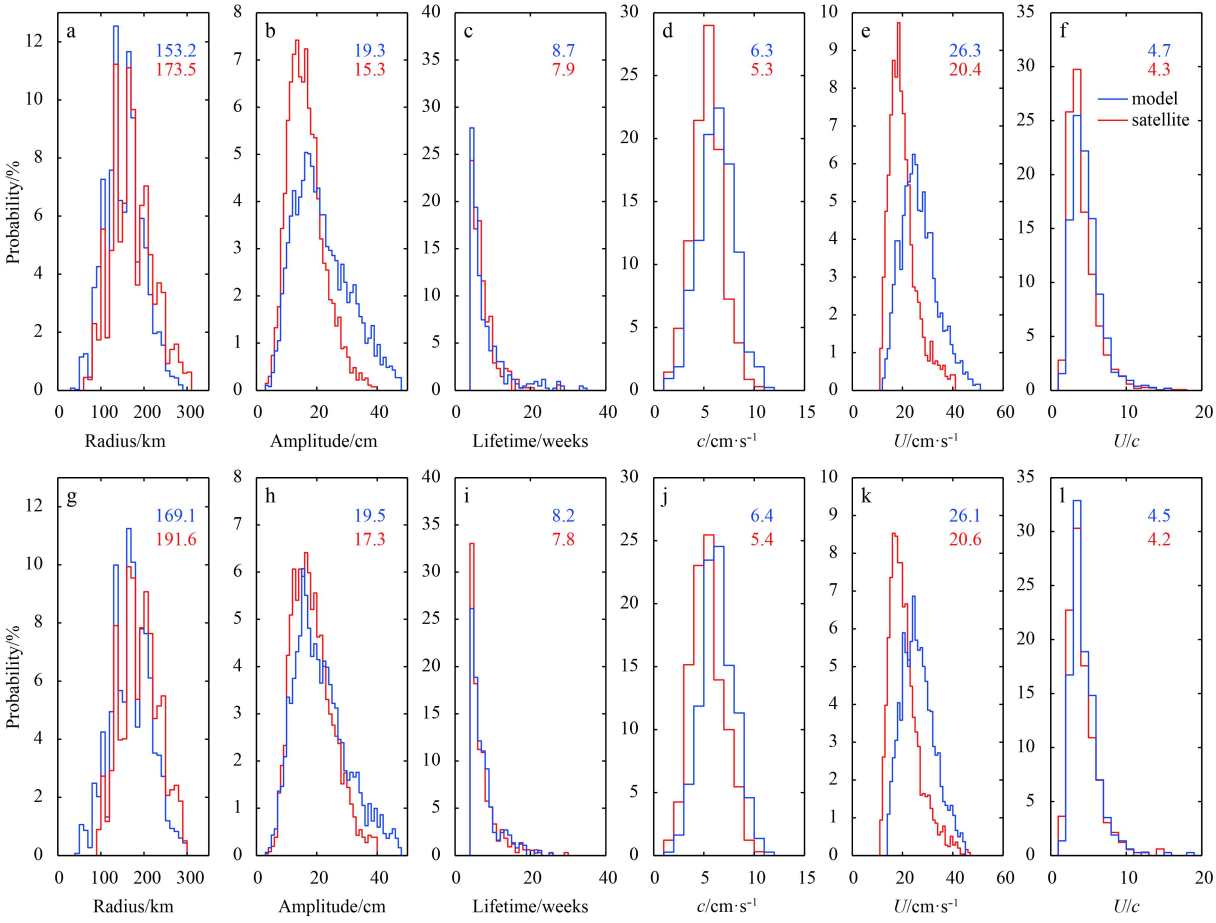

Fig. 5. The probability density function of the radius (a), amplitude (b), lifetime (c), translate speed (d), rotation speed (e) and nonlinear properties (f) for CEs based on the entire basin in the top panel. The red line and the blue line refer to the satellite and model, respectively. The same as the top panel but for AEs in the bottom panel.

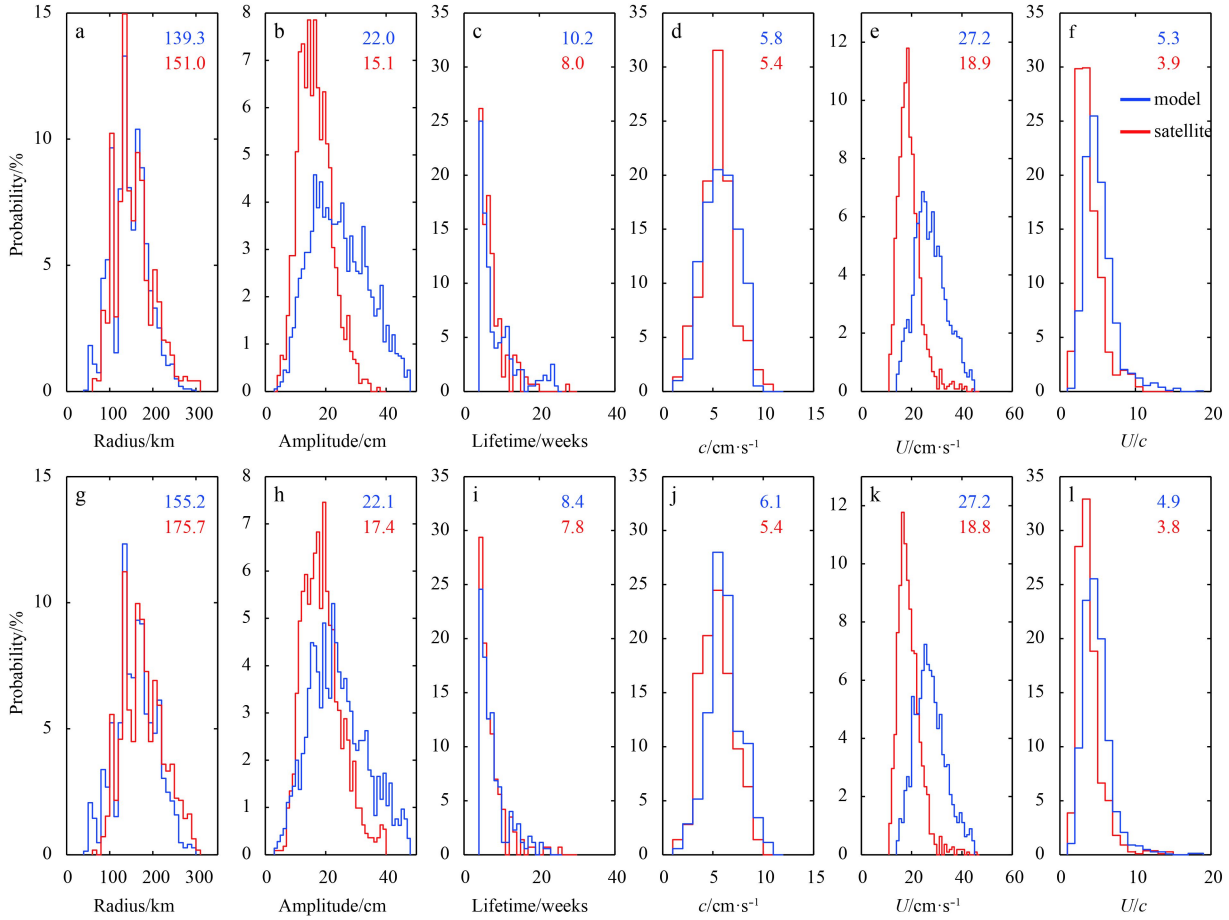

Fig. 6. The probability density function of the radius (a), amplitude (b), lifetime (c), translate speed (d), rotation speed (e) and nonlinear properties (f) for CEs based on the north area in the top panel. The red line and the blue line refer to the satellite and model, respectively. The same as the top panel but for AEs in the bottom panel.

The PDFs of the eddy amplitude also had a Rayleigh distribution for both the satellite and model (Figs 5b, 5h, 6b, 6h, 7b, and 7h). The simulated eddies were obviously stronger than those of the satellite data. The PDF range of the eddy simulated by the model was greater than that for the satellite. For example, CEs (AEs) for the entire basin with amplitudes higher than 40 cm accounted for 4.0% (3.7%) of all detected eddies in the model; however, no eddies with amplitudes larger than 40 cm appeared in the satellite data (Figs 5b and h). The PDF of the eddy amplitude in the NA showed similar features, and the amplitude in the model was even greater (Figs 6b and h). However, the amplitude difference between the model and satellite in the SA was not as large as that in the NA. The simulated mean amplitude of AEs in the SA was even smaller than that for the satellite data. Thus, the eddy amplitude features of the model for the entire basin may have been influenced mainly by eddies in the NA, which is greatly affected by the extremely strong Kuroshio intrusion. We also determined that the number of strong eddies with amplitudes greater than 25 cm was significantly higher for the model than that for the satellite data at 168 and 52, respectively. The strong eddies in the model occurred along the continental shelf (Figs 8c and d), whereas those in the satellite data were primarily to the east of Vietnam.

Regarding CEs in the entire basin, the PDFs of the lifespans of the 675 eddy trajectories for satellite and 799 for the model are shown in Fig. 5c. The lifetimes of the eddies were generally 5–15 weeks. Eddies with lifetimes longer than 20 weeks were infrequent, at 1.6% for satellite and 4.3% for the model. The latter mainly occurred in the NA (Figs 8e and f). It is clear that eddies with significantly longer lifetimes in the model led to a larger mean value of the total lifespan. The period mean simulated lifetime, 8.7 weeks, is slightly longer than that of the satellite data at 7.9 weeks. Again, the characteristics for the NA dominated those for the basin. The lifetimes for the model in the SA were even smaller than those for the satellite data.

The PDF of the eddy moving speed for CEs is shown in Figs 5d, 6d, and 7d for the entire SCS basin and the NA and SA, respectively. The observational estimations are all approximately 5.3–5.4 cm/s in the three regions. In general, the moving speeds of the eddies in the model were greater than those of the satellite in all three regions. The simulated mean value in the SA, 7.1 cm/s, is significantly faster than that of the satellite data at 5.3 cm/s. Eddy rotation speed, another important property, can be roughly characterized as being proportional to the ratio of the eddy amplitude to the eddy radius. Thus, considering the amplitude and radius analysis given above, it is not surprising that the eddies in model have faster rotation speeds for CEs compared with the satellite data in all areas, as shown in Figs 5e, 6e and 7e. Similar to that with the combination of radius and amplitude, the PDFs of the rotation speed also followed Rayleigh distribution. However, the rotation speed in the NA for the model was relatively larger than that for satellite, although the discrepancies in

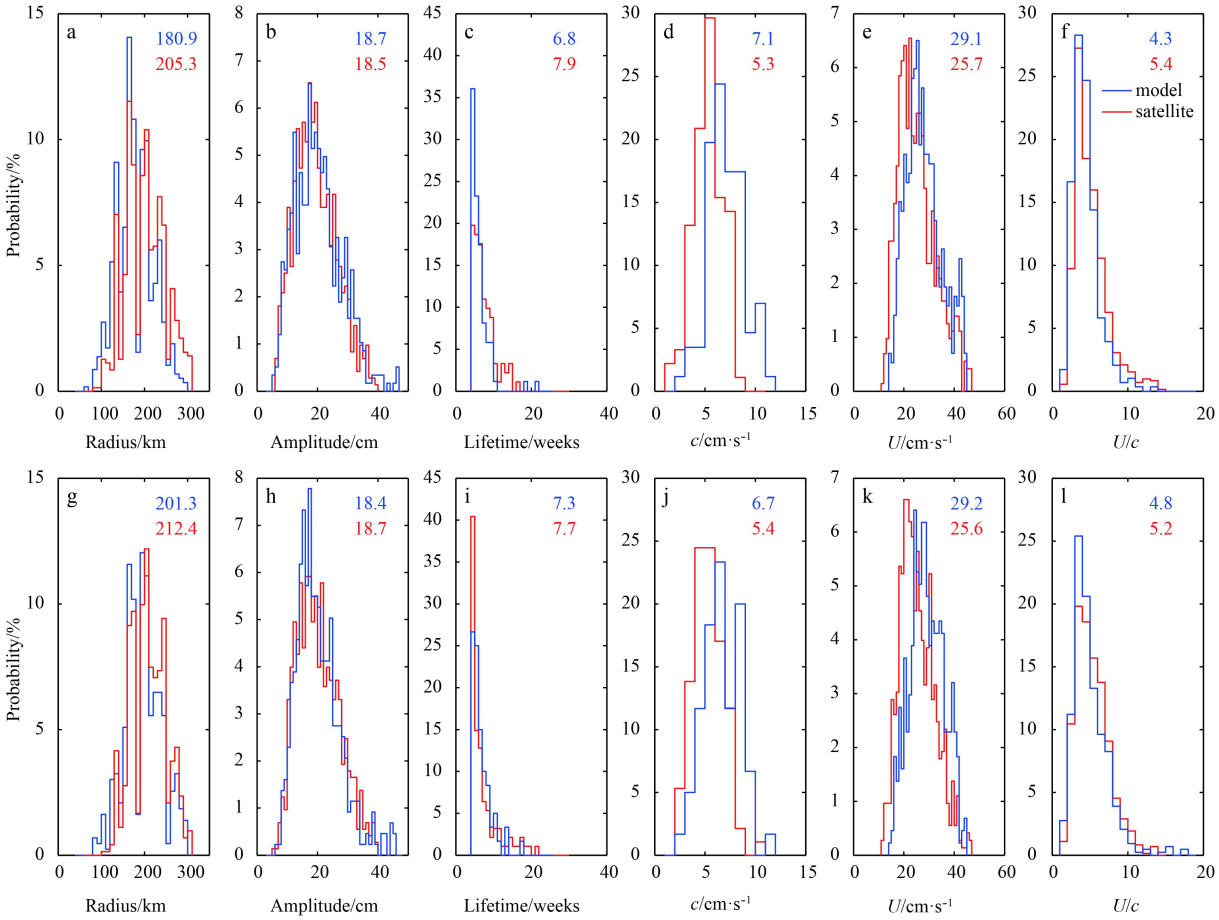

Fig. 7. The probability density function of the radius (a), amplitude (b), lifetime (c), translate speed (d), rotation speed (e) and nonlinear properties (f) for CEs based on the south area in the top panel. The red line and the blue line refer to the satellite and model, respectively. The same as the top panel but for AEs in the bottom panel.

the SA were not as large.

On the basis of the moving and rotation speed analyses given above, we can compute an additional eddy property: the nonlinear parameter (U/c). Considering the entire basin, the nonlinear parameter of eddies in the model was slightly larger than that in the satellite data. Thus, in the NA, the model nonlinear parameter was larger due to the significantly faster rotation speed (U), while the moving speed (c) for the model is same as that for the satellite. In the SA, however, the model parameter was smaller than that in the satellite due to the relatively faster moving speed and slower rotation speed. The moving speed, rotation speed, and nonlinear parameter features for AEs were similar to those for CEs.

In addition to moving speed, moving direction is also an important eddy parameter. Figure 9 shows the distribution of the average meridional azimuths, which is defined by the angle of the line between the generation and termination location relative to the latitude, of the CEs and AEs for both the satellite and model.

The proportions of eddies that propagated with equatorward deflection were dominant for both the satellite and model (Fig. 9). For CEs (AEs), the equatorward proportions were 53.7% (52.5%) for the satellite and 53.9% (59.8%) for the model. Therefore, little difference was detected between the model and the satellite. Previous observational studies have shown that CEs and AEs have distinct affinities for poleward and equatorward deflection, respectively (Chelton et al., 2007). Our results show tendency of equatorward deflection for AEs for both the satellite and model but no preference poleward deflection for CEs. Because the basin of SCS is relatively small, the northeast-southwest direction mean current in the NA region dominate, and then the trajectories of the eddies will follow the current, moving from northeast to southwest. Therefore, the deflection of the eddies is not same as that in open ocean. In the NA, the equatorward deflection of CEs and AEs was similar to that in the entire SCS basin although the proportions were significantly larger, particularly for the model results (not shown). The proportions of the equatorward deflection for both CEs and AEs exceeded 60%. In the SA, however, the proportions of the two directions were close to 50% for both the satellite and the model (not shown). We also computed the proportion of eddies moving westward and eastward (not shown). Almost 90% of the eddies showed westward movement; however, this topic will not be further discussed here.

The relationships among the three primary characteristics, including lifetime, radius, and amplitude, are shown in Fig. 10; the upper (lower) panel pertains to CEs (AEs). The patterns of the CEs and AEs are highly similar. The relationship between lifetime and radius is not as clear, however (Figs 10a and d). The eddies with lifetimes greater than 20 weeks generally has radii between 150 km and 200 km; however, those for the AEs were between approximately 100 km and 250 km. The amplitude increased with an increase in radius for both the satellite and mod-

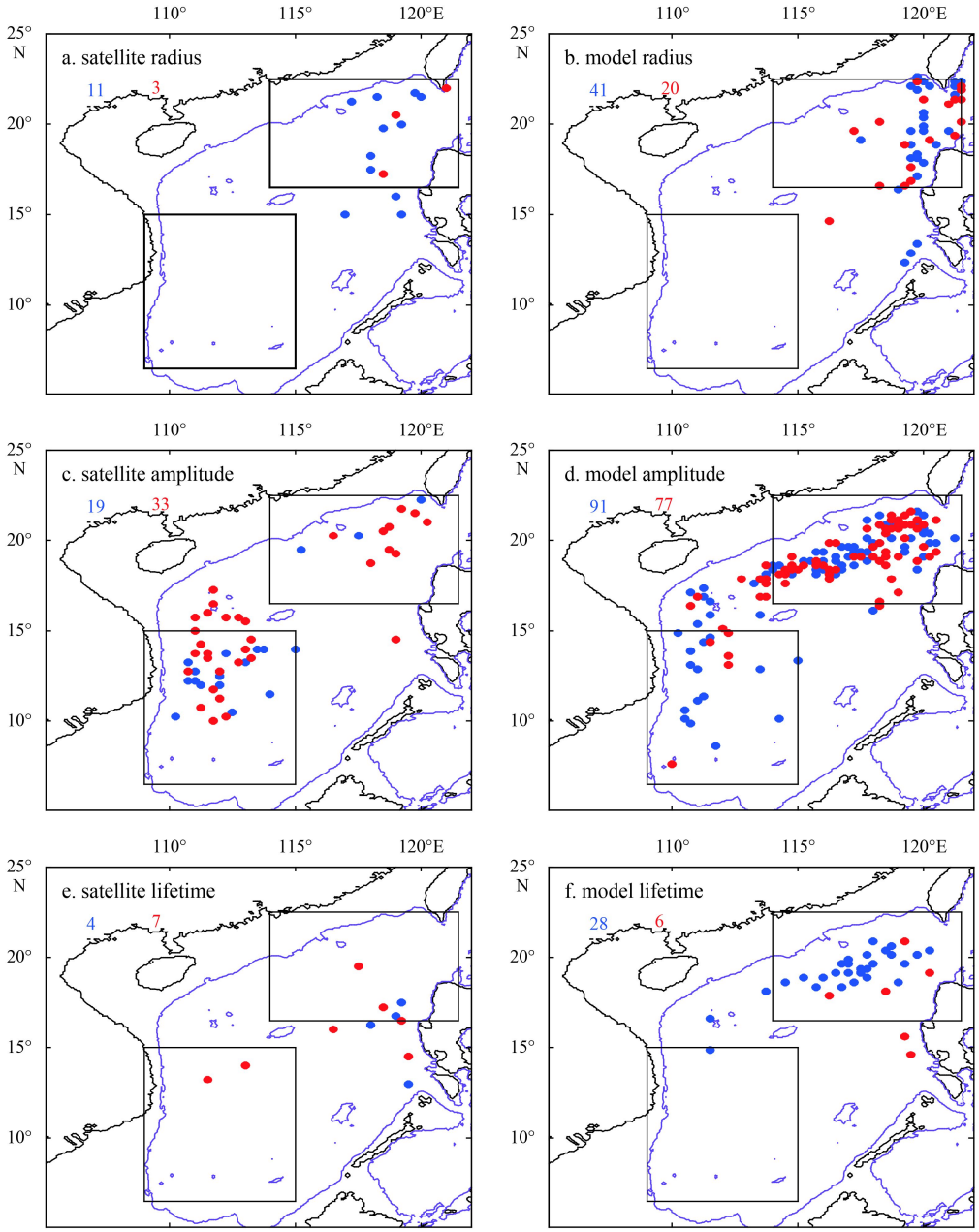

Fig. 8. The spatial distribution and numbers of CEs and AEs for the satellite and model with radius smaller than 100 km and greater than 50 km (a, b), amplitude greater than 25 cm (c, d) and lifetime greater than 20 weeks (e, f).

el (Figs 10b and e). However, the tendency rate of the model is obviously larger than that of the satellite data; that is, the amplitude of eddies in the model was significantly more sensitive than that for the satellite data. The amplitude and lifetime had no clear relationship (Figs 10c and f). For satellite data, both CEs and AEs had lifetimes greater than 20 weeks with amplitudes between 14 cm and 24 cm. With the exception of two eddies, the same characteristics for AEs were noted in the model; however, the model showed more than 10 CEs with lifetimes greater than 20 weeks and amplitudes larger than 30 cm.

According to the analysis given above, the model appears to be more energetic than the satellite in the entire SCS basin; however it is inhomogeneous in the spatial distribution. Eddies are significantly more active in the NA than in the SA, where the amplitude, lifetime, and nonlinear parameters for the model were all larger than those for the satellite. In addition to the small viscosity mentioned in the previous subsection, the extreme intrusion of the Kuroshio in the Luzon Strait is likely attributed to the errors in simulated eddy properties in the NA. The strong intrusion may also affect the boundary currents off the coast of Vietnam and thus eddies in the SA.

4.3 *Seasonal variability*

The upper-layer circulation of the SCS is dominated by monsoons (Fang et al., 1998; Qu et al., 2000; Hu et al., 2000). Therefore, both the mean currents and MEs can be affected by monsoons, as shown in Figs 1 and 2. In this section, we discuss the seasonal variations of eddy numbers and amplitude in detail.

Figure 11 shows the generation numbers of CEs and AEs in four seasons, defined as a three-month average, such as Decem-

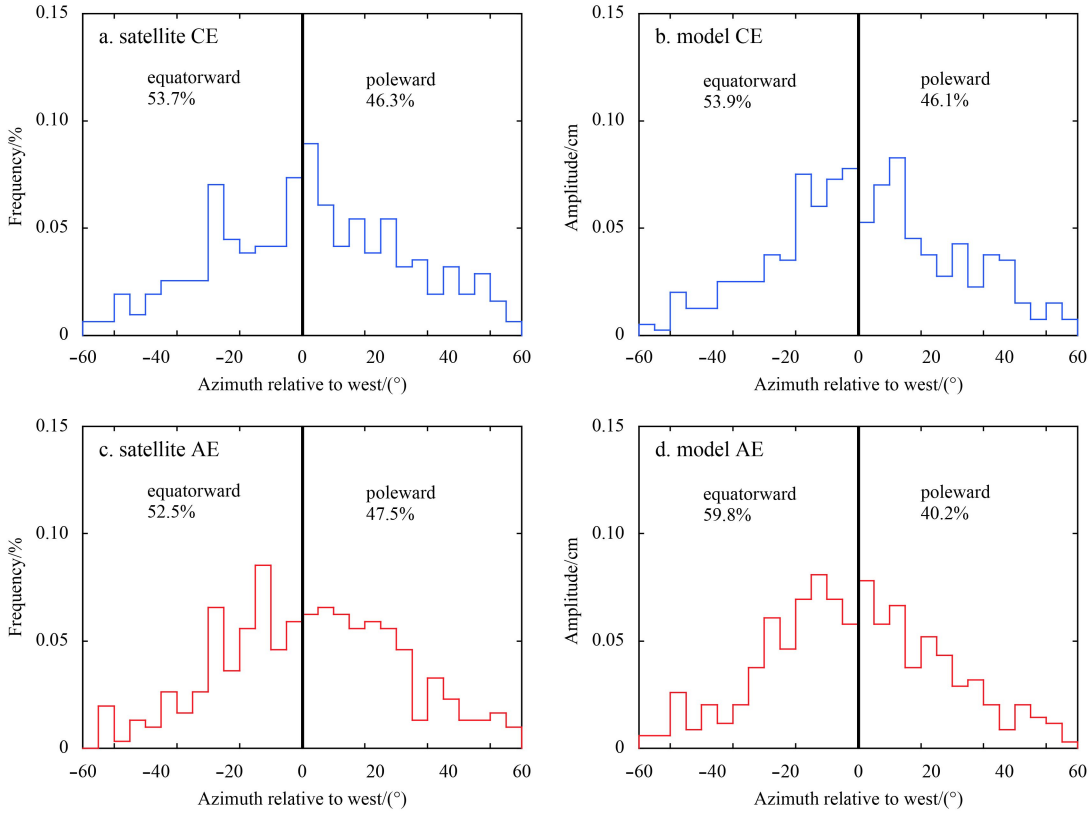

Fig. 9. The distributions of the average azimuths of the trajectories of the satellite data and the model data of the CEs (a, b) and the AEs (c, d).

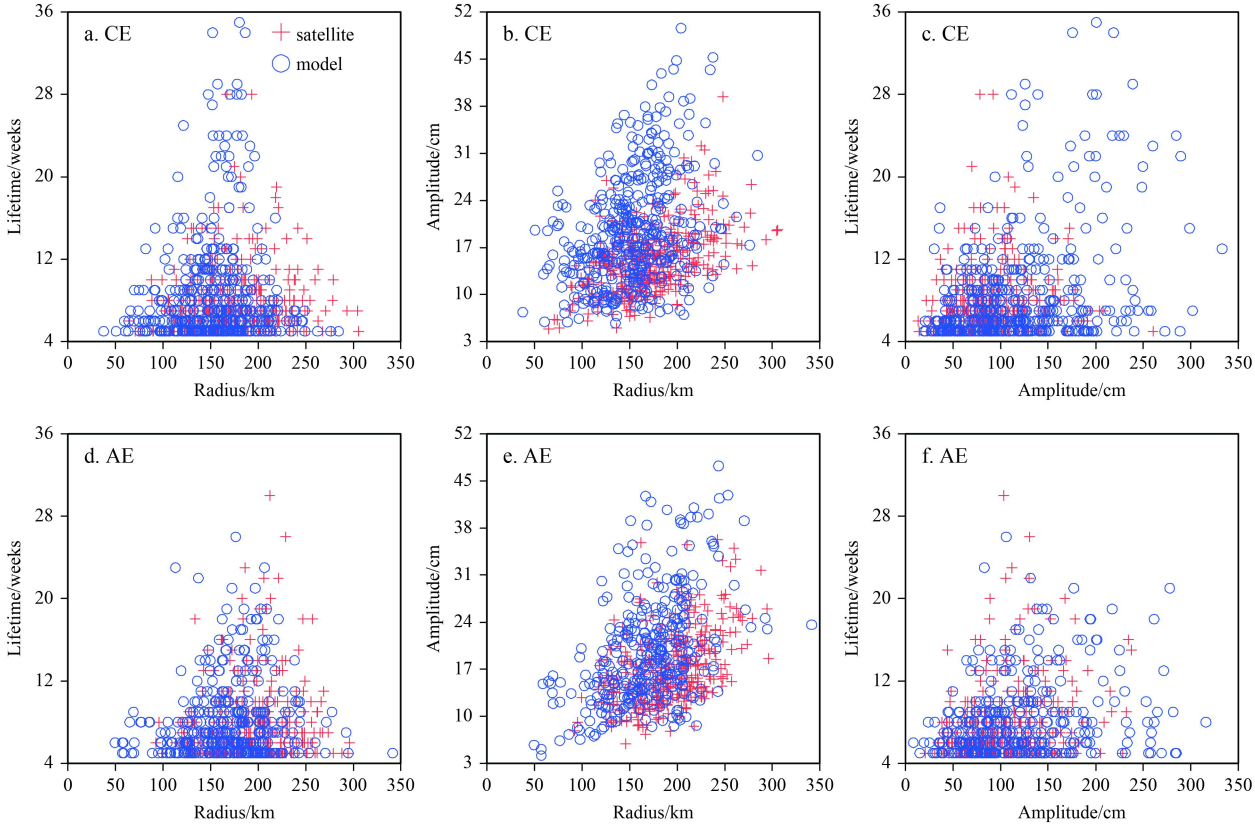

Fig. 10. Relations between the radius and lifetime (a, d), radius and amplitude (b, e) and amplitude and lifetime (c, f) of CEs (top panel) and AEs (lower panel), respectively. The blue and red dots refer to the satellite and model, respectively.

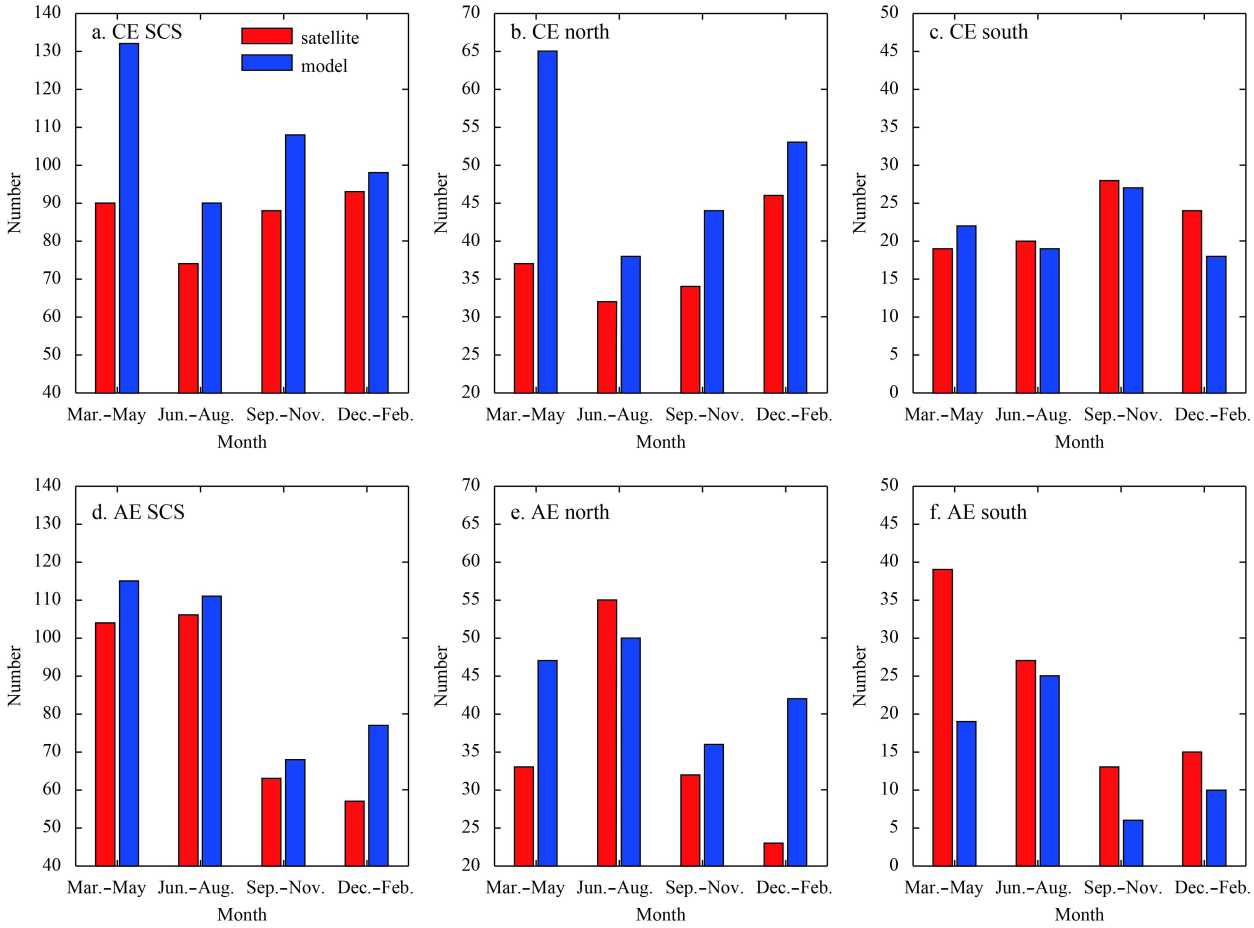

Fig. 11. The seasonal cycle of generation eddy numbers of satellite and model for CEs and AEs based on the entire basin (a, d), north area (b, e) and south area (c, f). The red and blue color refers to the satellite and model, respectively.

ber–January–February, for both the satellite and model in the entire SCS basin and the NA and SA, respectively. In the satellite, the eddy generation number has significant seasonal variability in the SCS (Figs 11a and d); the phases of the seasonal cycles for AEs and CEs are different. For the entire SCS basin and the NA, the largest (smallest) number of CEs occurs in winter (summer); the opposite is true for AEs. The peaks and troughs of eddy numbers occur in the transient seasons in the SA with the peak in fall (spring) and trough in spring (fall) for CEs (AEs). In general, a significantly greater (lower) number of MEs in the NA (SA) were simulated by LICOM2.0. For CEs (Figs 11a, b and c), the largest positive number bias occurred in spring for both the entire basin and the NA. The number of CEs in the NA was nearly double that in spring in the model; in other seasons, however, the differences were relatively small in the NA. For AEs (Figs 11d, e and f), the large biases were not detected in the entire basin. However, large negative bias was found in the SA, also in the spring season. These biases interfere with the seasonal cycle of the model.

We also investigated the seasonal variability of amplitude of the MEs. Figure 12 shows the seasonal cycle of eddy amplitude based on the entire basin and the NA and SA. The model tended to reproduce strong MEs in most parts of the SCS. The phases of variability were also simulated very well in the model. It is interesting to note that the model simulated weak CEs during summer and fall in the SA.

To understand the causes of the biases in eddy generation number in spring, the surface currents for both the satellite and the model in spring (March–April–May, MAM) were investigated (Figs 13a and b). It is evident that the Kuroshio intrusion in LICOM2.0 was significantly stronger than that in the observation. The Kuroshio intrusion flows to the west from the Luzon Strait to the western boundary of the SCS in LICOM2.0. Then, the flow turns southward and reaches as far south as approximately 13°N after turning eastward; the flow turned eastward at approximately 16°N in the observation. The enhanced northern circulation in LICOM2.0 pushes the southern circulation farther south. The northern part of the SCS is more strongly affected by the Kuroshio intrusion in the model and leads more energetic conditions.

As reported in previous studies, the eddy generations in the SCS are dominated by barotropic and baroclinic instability (e.g., Yang et al., 2013). We investigated the barotropic instability by using the vortices of the surface velocity, which also decide the polarity of the eddy. It is evident that changes in the general circulation pattern will change the pattern and magnitude of the horizontal shear of the velocity. Figures 13c and d show the vortices of the surface currents for both the satellite and the LICOM during MAM. The most notable feature of the vortices in the model is the enhanced positive and negative band north of 15°N (Figs 13c and d) related to both the exaggerated Kuroshio intrusion and a strong recirculation just south (Fig. 13b). Such conditions lead to strong positive vortices west of the Luzon Strait (Fig. 13d), which favor the generation of CEs. The enhanced northern circulation in LICOM2.0 also pushes the southern circulation

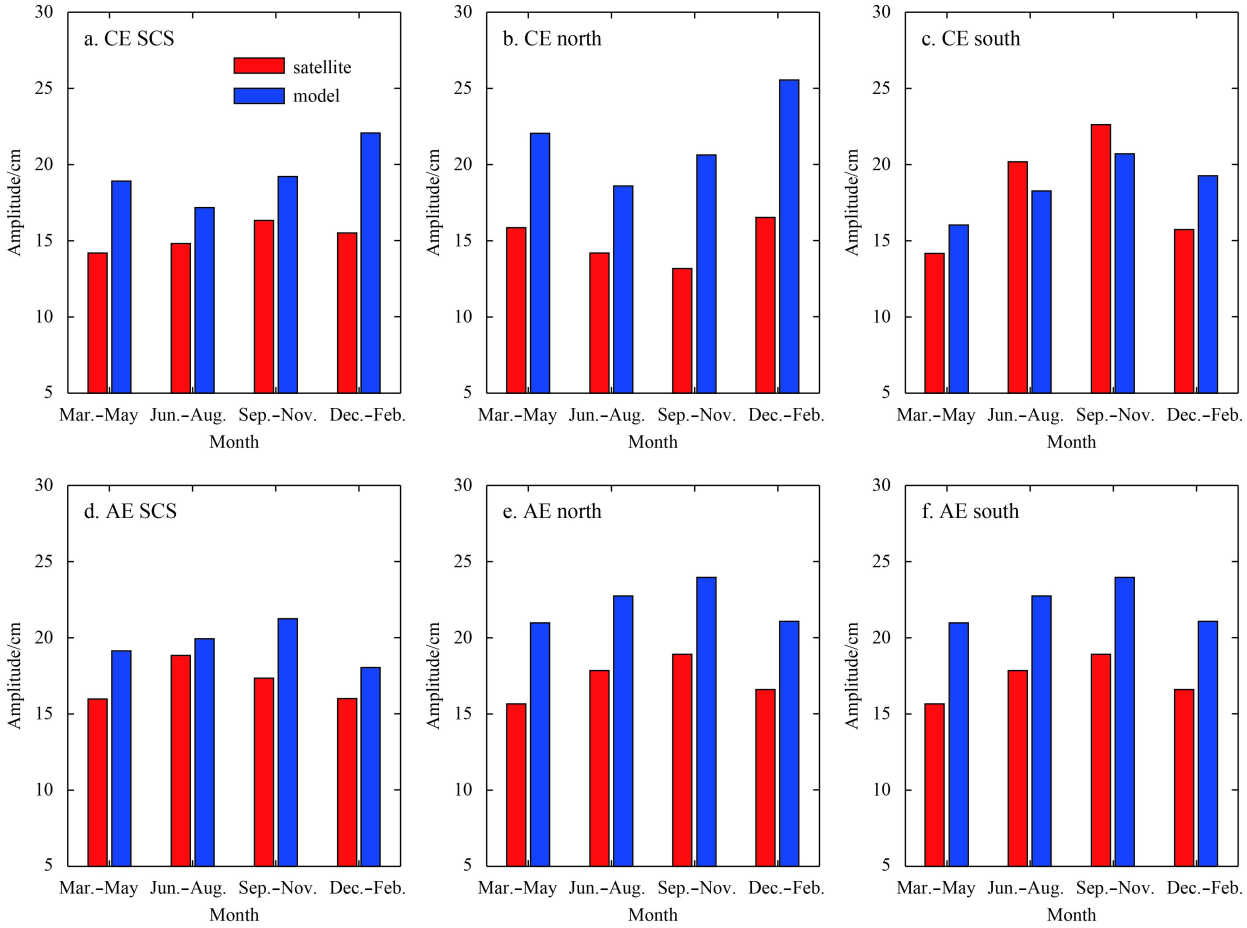

Fig. 12. The seasonal cycle of eddy amplitude of satellite and model for CEs and AEs based on the entire basin (a, d), north area (b, e) and south area (c, f). The red and blue color refers to the satellite and model, respectively.

farther south and changes the pattern of the vortices in the SA (Figs 13c and d). The negative vortex center for LICOM in the SA is much weaker and more southward than that for the satellite data. This result leads to the negative vortices dominant the SA in LICOM2.0 rather than the positive vortices in the observation.

We further investigated the area-averaged vertical velocity shear and the stratification within the NA and the SA, which are generally used to measure baroclinic instability (Fig. 14). As shown in Fig. 13, the exact regions are the Kuroshio intrusion inflow area with two northern points, 22°N, 120.5°E; 19.5°N, 114°E, and two southern points, 16°N, 114.5°E; 18.5°N, 121°E, in addition to east offshore Vietnam (12°–16.5°N, 109.5°–113°E). Here we used the reanalysis data from the Simple Ocean Data Assimilation (SODA) version 2.0.2–4 as an observational reference. The conditions in the two regions were nearly the same. The simulated vertical shears in both the NA and SA were larger than that for SODA, particularly in the upper 200 m. The simulated stratifications in the two regions were smaller than that for SODA, except for 20–100 m. The larger vertical velocity shear and small buoyancy frequency both tend to reveal more eddies in the model. The baroclinic instability appears to conflict with the above analysis by showing fewer eddies in the SA. We consider three possible reasons. The first is that barotropic instability is dominant in this region; the second is that many eddies may be filtered out by the criteria of our identification method, such as eddy sizes larger than 50 km and lifetimes longer than four weeks. Thus, the mechanism of eddy generation in the model needs further investigation in our future studies. The third is that the resolution of the observational reference we choose, SODA, may be not high to evaluate those processes.

The above analysis of the seasonal variability shows that the largest bias in both the NA and SA occurs in spring, which is the transient season of the monsoon. The model tends to simulate a significantly greater number of CEs in the northern part of the SCS and fewer AEs in the southern part. During this season, the surface wind as well as the wind curl is weak, the intrinsic processes dominate the eddy generation. Because the external forcing usually comes from the observation, that is, it has much less bias than that in the intrinsic processes. Therefore, there are much more biases in the model during this season.

We also computed the T2 and T4 terms by using the model data following Zhuang et al. (2010) (figure not shown). We can find the energy is transferred from mean flow to eddies (positive values) in our model, especially in the west of the Luzon Strait and along the coast of Vietnam. It is further confirmed our analysis above that the change of mean flow can affect the eddy generation significantly.

5 Concluding remarks

In the present study, the numbers and properties of MEs in the SCS simulated by an eddy-resolving ocean general circulation model, as well as their seasonal variability, are evaluated against satellite data recorded during 1993–2007 by using eddy detection and tracking methods of Lin et al. (2007). The main

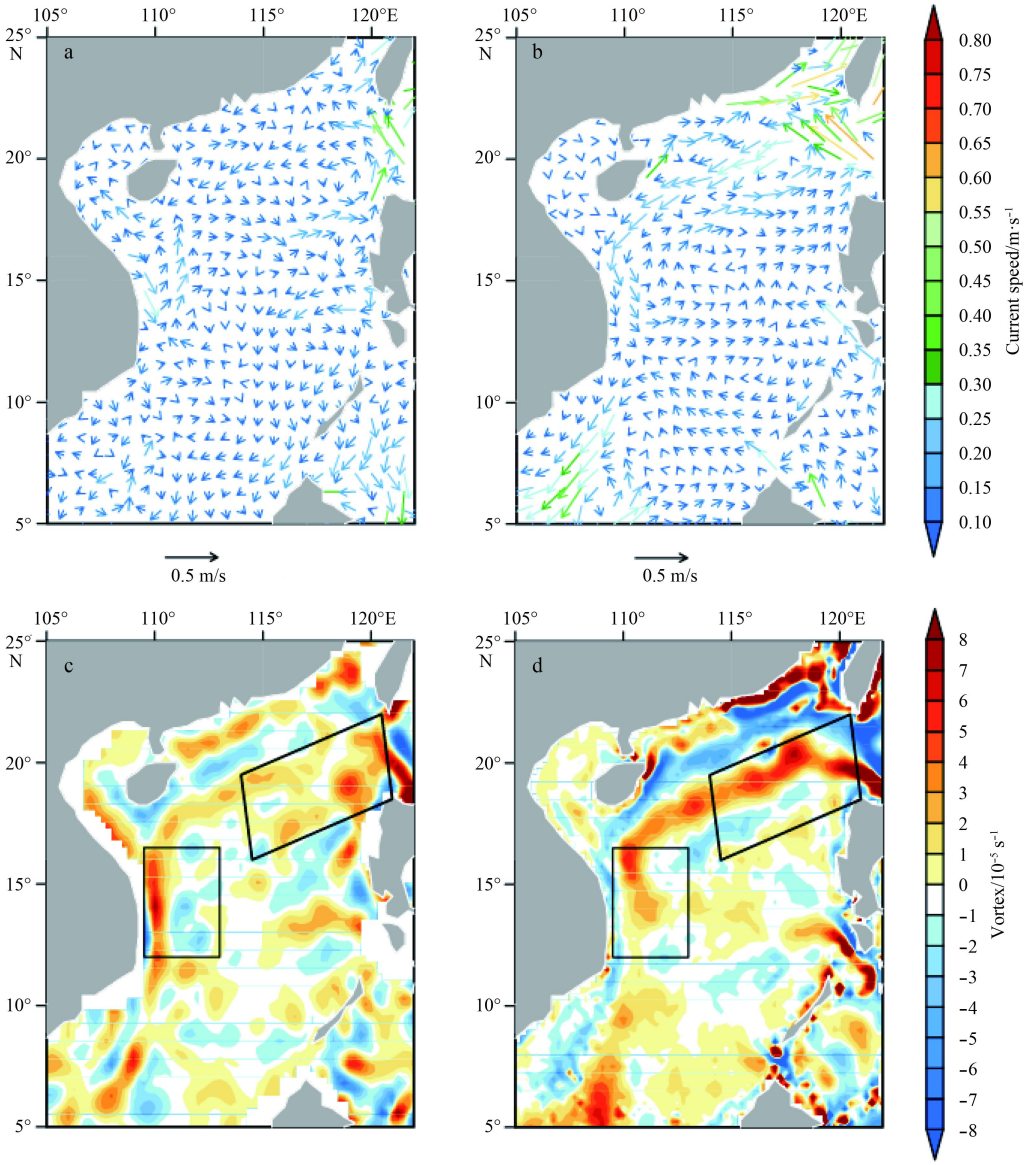

Fig. 13. The upper layer geostrophic current in spring of the satellite (a) and model (b) and the spring surface vortex of satellite (c) and model (d). The shaded in (a) and (b) refers to the speed magnitude of the current and the unit is m/s. The unit of the vortex is in 10^{-5}/s.

conclusions are as follows:

(1) LICOM generally tends to reproduce more eddies in the SCS. A total of 345 CEs and 330 AEs generated for satellite data and 428 CEs and 371 AEs generated for model data are identified during the study period, showing increases of approximately 24% and 12%, respectively. However, the spatial distribution is inhomogeneous with more CEs in the northern part of the SCS and fewer AEs in the southern part.

(2) For the entire basin, the MEs simulated by the model, whether AEs or CEs, tend to have smaller radii, larger amplitudes, slightly longer lifetimes, faster moving and rotation speeds, and slightly larger nonlinear properties (U/c) than those of the satellite data. The small eddies in the model occur just west of the Luzon Strait, and the fast-moving eddies with long lifetimes appear mainly in the northern part along the continental shelf.

(3) The seasonal variability in the eddy generation number shows that the largest bias in both the NA and SA occurs in spring, with a significantly greater number of CEs in the NA and fewer AEs in the SA. During this season, the surface wind as well as the wind curl is weak, the intrinsic processes dominate the eddy generation. Because the external forcing usually comes from the observation, that is, it has much less bias than that in the intrinsic processes. Therefore, there are much more biases in the model during this season.

In present study, the most evident model bias appears to be the significantly higher number of eddies with greater strength than that identified in the satellite data. That is, the model is more energetic than the observational data. However uncertainties may remain in the satellite data, which may affect the robustness of the conclusion. The horizontal resolution of AVISO data (~25 km) is capable of eddy resolution for the entire SCS basin except for the continental shelf. Therefore, the number of MEs may be underestimated by the satellite data. Data with significantly higher resolution are required to further evaluate the model.

In addition to the higher energy of the ocean in the model, the spatial distribution of both the numbers and other features such as radius, lifetime, and magnitude are inhomogeneous. Larger biases appear in the number, magnitude, and moving speed of MEs in the NA than those in the SA. All of the analysis shows that the biases in the NA may be related to the extremely strong Kuroshio intrusion through the Luzon Strait, in which the small islands have not been represented well. To determine whether corrected biases in the Kuroshio intrusion result in a reduction in ME biases, two sensitivity experiments have been conducted. The first uses the same topography as that in the control run (Exp1, it is basically the same as the model used above, although the running time is a little short), and the other uses modified topography (Exp2), in which the islands in the middle and southern parts of the Luzon Strait have been added manually. The simulated Kuroshio intrusion in the model shows significant improvement in Exp2 (Figs 15a and b). Moreover, as shown in Table 1, the number of CEs in the NA is reduced from 50 to 37, and the number of AEs in the SA is increased from 7 to 10. Meanwhile, the number of eddies generated in the SA is increased from 21 to 35 and it is obviously improved the situation that less eddies generated in the SA for model. The difference of eddy number between the NA and SA has been much reduced from 54 for Exp1 to 35 for Exp2. In a word, Exp2 showed less eddies in the NA and more eddies in the SA, which is more approximately to the satellite. The sensitivity experiments further confirm our speculation. However, their detailed analysis will be presented in a separate paper.

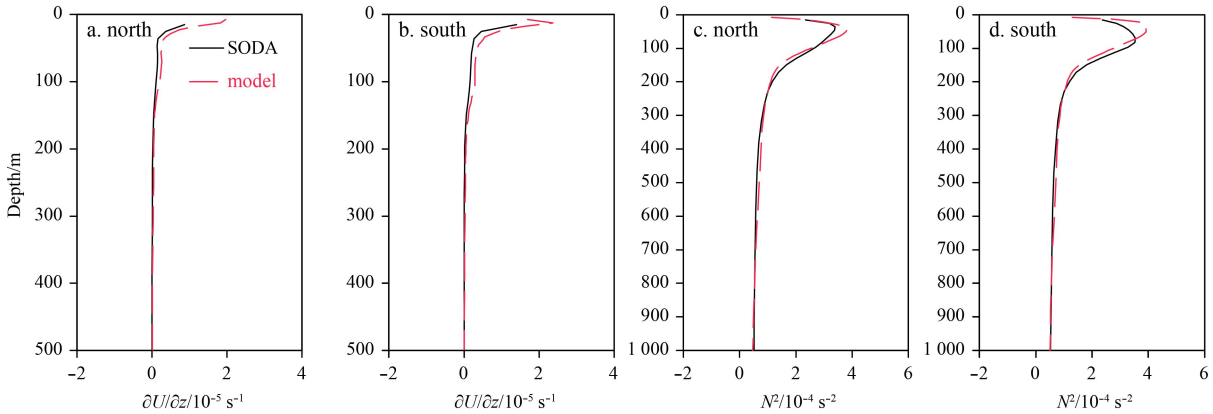

Fig. 14. The mean vertical variation of the total current speed squared (a) and buoyancy frequency squared (b) in the Kuroshio inflow area and the east offshore of the Vietnam (averaged within the black box in Fig. 11) in spring for SODA and model. The black line and the red line refer to the satellite and model, respectively.

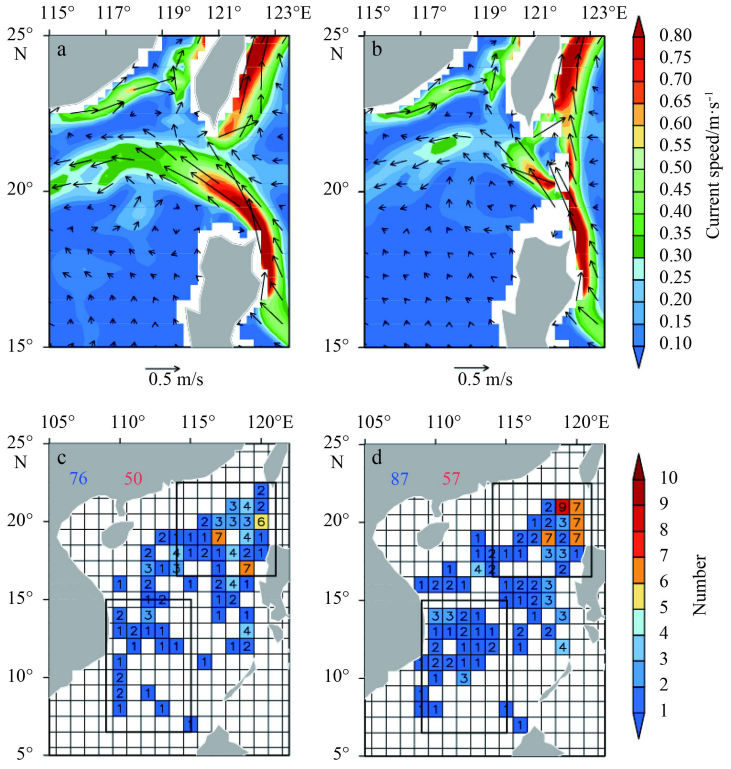

Fig. 15. The upper layer circulation in the northern of the SCS especially for the Luzon Strait for the Exp1 (a) and Exp2 (b). The shaded refers the magnitude of the current velocity and the unit is m/s. Regional climatology of eddy genesis for the Exp1 (c) and Exp2 (d).

An additional interesting problem is that large biases occur mainly in spring. We consider that because of the weak wind in that season, generation of MEs is dominated by intrinsic processes rather than external forcing. The biases in the extreme Kuroshio intrusion may also affect the seasonality of the biases in MEs. However, these speculations require further investigation.

References

Chaigneau A, Eldin G, Dewitte B. 2009. Eddy activity in the four major upwelling systems from satellite altimetry (1992–2007). Progress in Oceanography, 83(1–4): 117–123

Chaigneau A, Gizolme A, Grados C. 2008. Mesoscale eddies off Peru in altimeter records: identification algorithms and eddy spatio-temporal patterns. Progress in Oceanography, 79(2–4): 106–119

Chelton D B, Schlax M G, Samelson R M. 2011. Global observations of nonlinear mesoscale eddies. Progress in Oceanography, 91(2): 167–216

Chelton D B, Schlax M G, Samelson R M, et al. 2007. Global observations of large oceanic eddies. Geophysical Research Letters, 34(15): L15606

Chen Gengxin, Gan Jianping, Xie Qiang, et al. 2012. Eddy heat and salt transports in the South China Sea and their seasonal modulations. Journal of Geophysical Research: Oceans (1978–2012): 117(C5): doi: 10.1029/2011JC007724

Chen Gengxin, Hou Yijun, Chu Xiaoqing. 2011. Mesoscale eddies in the South China Sea: mean properties, spatiotemporal variability, and impact on thermohaline structure. Journal of Geophysical Research: Ocean (1978–2012), 116(C6): doi: 10.1029/2010JC006716

Chen Gengxin, Hou Yijun, Zhang Qilong, et al. 2010. The eddy pair off eastern Vietnam: interannual variability and impact on thermohaline structure. Continental Shelf Research, 30(7): 715–723

Chen Gengxin, Wang Dongxiao, Dong Changming, et al. 2015. Observed deep energetic eddies by seamount wake. Scientific Report, 5: 17416, doi: 10.1038/srep17416

Chen Gengxin, Xue Huijie, Wang Dongxiao, et al. 2013. Observed near-inertial kinetic energy in the Northwestern South China Sea, Journal of Geophysical Research: Ocean (1978–2012), 118(10): doi: 10.1002/jgrc.20371

Cheng Xuhua, Qi Yiquan. 2010. Variations of eddy kinetic energy in the South China Sea. Journal of Oceanography, 66(1): 85–94

Chow C H, Liu Qinyu. 2012. Eddy effects on sea surface temperature and sea surface wind in the continental slope region of the northern South China Sea. Geophysical Research Letters, 39(2): doi: 10.1029/2011gl050230

Chu Xiaoqing, Xue Huijie, Qi Yiquan, et al. 2014. An exceptional anticyclonic eddy in the South China Sea in 2010. Journal of Geophysical Research, 119(2): 881–897, doi: 10.1002/2013JC009314

Ducet N, Le Traon P Y, Reverdin G. 2000. Global high-resolution mapping of ocean circulation from TOPEX/Poseidon and ERS-1 and -2. Journal of Geophysical Research: Oceans (1978–2012), 105(C8): 19477–19498

Fang Guohong, Fang Wendong, Fang Yue, et al. 1998. A survey of studies on the South China Sea upper ocean circulation. Acta Oceanographica Taiwanica, 37(1): 1–16

Gan Jianping, Qu Tangdong. 2008. Coastal jet separation and associated flow variability in the southwest South China Sea. Deep Sea Research Part I: Oceanographic Research Papers, 55(1): 1–19

Gent P R, McWilliams J C. 1990. Isopycnal mixing in ocean circulation models. Journal of Physical Oceanography, 20(1): 150–155

Hallberg R. 2013. Using a resolution function to regulate parameterizations of oceanic mesoscale eddy effects. Ocean Modelling, 72: 92–103

Hu Jianyu, Kawamura H, Hong Huasheng, et al. 2000. A review on the currents in the South China Sea: seasonal circulation, South China Sea warm current and Kuroshio intrusion. Journal of Oceanography, 56(6): 607–624

Isern-Fontanet J, García-Ladona E, Font J. 2003. Identification of marine eddies from altimetric maps. Journal of Atmospheric and Oceanic Technology, 20(5): 772–778

Isern-Fontanet J, García-Ladona E, Font J. 2006. Vortices of the Mediterranean Sea: an altimetric perspective. Journal of Physical Oceanography, 36(1): 87–103

Jia Yinglai, Liu Qinyu, Liu Wei. 2005. Primary study of the mechanism of eddy shedding from the Kuroshio bend in Luzon Strait. Journal of Oceanography, 61(6): 1017–1027

Large W G, Yeager S G. 2004. Diurnal to decadal global forcing for ocean and sea-ice models: the data sets and flux climatologies. NCAR Technical Note NCAR/TN-460+STR. Colorado: National Center for Atmospheric Research Boulder, 111

Li Li, Nowlin Jr W D, Su Jilan. 1998. Anticyclonic rings from the Kuroshio in the South China Sea. Deep Sea Research Part I: Oceanographic Research Papers, 45(9): 1469–1482

Lin Xiayan, Dong Changming, Chen Dake, et al. 2015. Three-dimensional properties of mesoscale eddies in the south china sea based on eddy-resolving model output. Deep Sea Research Part I: Oceanographic Research Papers, 99: 46–64

Lin Pengfei, Wang Fang, Chen Yongli, et al. 2007. Temporal and spatial variation characteristics on eddies in the South China Sea: I. Statistical analyses. Haiyang Xuebao (in Chinese), 29(3): 14–22

Liu Qinyu, Kaneko A, Su Jilan. 2008. Recent progress in studies of the South China Sea circulation. Journal of Oceanography, 64(5): 753–762

Liu Hailong, Lin Pengfei, Yu Yongqiang, et al. 2012. The baseline evaluation of lasg/iap climate system ocean model (LICOM) version 2. Acta Meteorologica Sinica, 26(3): 318–329

Liu Xiaobing, Su Jilan. 1992. A reduced gravity model of the circulation in the South China Sea. Oceanologia et Limnologia Sinica (in Chinese), 23(2): 167–174

Liu Hailong, Yu Yongqiang, Lin Pengfei, et al. 2014. High-Resolution LICOM. In: Zhou Tianjun, Yu Yongqiang, Liu Yimin, et al., eds. Flexible Global Ocean-Atmosphere-Land System Model. Berlin Heidelberg: Springer, 321–331

Metzger E J, Hurlburt H E. 2001. The nondeterministic nature of Kuroshio penetration and eddy shedding in the South China Sea. Journal of Physical Oceanography, 31(7): 1712–1732

Nan Feng, He Zhigang, Zhou Hui, et al. 2011. Three long-lived anticyclonic eddies in the northern South China Sea. Journal of Geographical Research: Oceans (1978–2012), 116(C5): C05002

Nencioli F, Dong Changming, Dickey T, et al. 2010. A vector geometry-based eddy detection algorithm and its application to a high-resolution numerical model product and high-frequency radar surface velocities in the Southern California Bight. Journal of Atmospheric and Oceanic Technology, 27(3): 564–579

Okubo A. 1970. Horizontal dispersion of floatable particles in the vicinity of velocity singularities such as convergences. Deep Sea Research and Oceanographic Abstracts, 17(3): 445–454

Petersen M R, Williams S J, Maltrud M E, et al. 2013. A three-dimensional eddy census of a high-resolution global ocean simulation. Journal of Geophysical Research: Oceans (1978–2012), 118(4): 1759–1774, doi: 10.002/jgrc.20155

Qu Tangdong. 2000. Upper-layer circulation in the South China Sea. Journal of Physical Oceanography, 30(6): 1450–1460

Qu Tangdong, Mitsudera H, Yamagata T. 2000. Intrusion of the North Pacific waters into the South China Sea. Journal of Geophysical Research: Oceans (1978–2012), 105(C3): 6415–6424

Roeske F. 2001. An atlas of surface flues based on the ECMWF re-analysis: a climatological dataset to force global ocean general circulation models. Report No. 323. Hamburg: Max-Planck-Institut für Meteorologie, 31

Shaw P T, Chao S Y, Fu L L. 1999. Sea surface height variations in the South China Sea from satellite altimetry. Oceanologica Acta, 22(1): 1–17

Souza J M A C, de Boyer Montégut C, Le Traon P Y. 2011. Comparison between three implementations of automatic identification algorithms for the quantification and characterization of mesoscale eddies in the South Atlantic Ocean. Ocean Science, 7(3): 317–334

Wang Dongxiao, Chen Ju, Chen Rongyu, et al. 2004. Hydrographic and circulation characteristics in middle and southern South

China Sea in summer, 2000. Oceanologia et Limnologia Sinica (in Chinese), 35(2): 97–109

Wang Guihua, Chen Dake, Su Jilan. 2008a. Winter eddy genesis in the eastern South China Sea due to orographic wind jets. Journal of Physical Oceanography, 38(3): 726–732

Wang Liping, Koblinsky C J, Howden S. 2000. Mesoscale variability in the South China Sea from the TOPEX/Poseidon altimetry data. Deep Sea Research Part I: Oceanographic Research Papers, 47(4): 681–708

Wang Guihua, Su Jilan, Chu P C. 2003. Mesoscale eddies in the South China Sea observed with altimeter data. Geophysical Research Letters, 30(21): 2121

Wang Dongxiao, Xu Hongzhou, Lin Jing, et al. 2008b. Anticyclonic eddies in the northeastern South China Sea during winter 2003/2004. Journal of Oceanography, 64(6): 925–935

Wang Qiang, Zeng Lili, Zhou Weidong, et al. 2015. Mesoscale eddies cases study at Xisha waters in the South China Sea in 2009/2010. Journal of Geophysical Research: Oceans (1978–2012), 120(1): 517–532, doi: 10.1002/2014JC009814

Weiss J. 1991. The dynamics of enstrophy transfer in two-dimensional hydrodynamics. Physica D: Nonlinear Phenomena, 48(2–3): 273–294

Wu C R, Chiang T L. 2007. Mesoscale eddies in the northern South China Sea. Deep Sea Research Part II: Topical Studies in Oceanography, 54(14–15): 1575–1588

Wu C R, Shaw P T, Chao S Y. 1999. Assimilating altimetric data into a South China Sea model. Journal of Geophysical Research: Oceans (1978–2012), 104(C12): 29987–30005

Xiu Peng, Chai Fei, Shi Lei, et al. 2010. A census of eddy activities in the South China Sea during 1993–2007. Journal of Geophysical Research: Oceans (1978–2012), 115(C3), doi: 10.1029/2009JC005657

Yang Haijun, Liu Qinyu. 1998. The seasonal features of temperature distributions in the upper layer of the South China Sea. Oceanologia et Limnologia Sinica (in Chinese), 29(5): 501–507

Yang Haiyuan, Wu Lixin, Liu Hailong, et al. 2013. Eddy energy sources and sinks in the South China Sea. Journal of Geophysical Research, 118(9): 4716–4726

Yu Yongqiang, Liu Hailong, Lin Pengfei. 2012. A quasi-global 1/10° eddy-resolving ocean general circulation model and its preliminary results. Chinese Science Bulletin, 57(30): 3908–3916

Zhuang Wei, Xie Shangping, Wang Dongxiao, et al. 2010. Intraseasonal variability in sea surface height over the South China Sea. Journal of Geophysical Research: Oceans (1978–2012), 115(C4): doi: 10.1029/2009JC005647